ECS Transactions, 78 (1) 1851-1863 (2017)
10.1149/07801.1851ecst ©The Electrochemical Society

Corrugated Electrode/Electrolyte Interfaces in SOFC: Theoretical and Experimental Development

A. Chesnaud[a], F. Delloro[a], M. Geagea[a], A. P. Abellard[a], J. Ouyang[b], D. Li[b], T. Shi[b], B. Chi[b], R. Ihringer[c], M. Cassir[d], and A. Thorel[a]

[a] Mines-ParisTech, PSL Research University, MAT-Centre des Matériaux
CNRS UMR 7633, Evry 91003, France
[b] HUST-Huazhong University of Science and Technology, ICARE Institute
Wuhan 430074, China
[c] Fiaxell Sàrl, PSE A, Science Park, Lausanne 1015, Switzerland
[d] Chimie-ParisTech, PSL Research University
CNRS UMR 8247, Paris 75231 Cedex 05, France

The present work proposes to explore how the presence of a periodic pattern at electrode/electrolyte interfaces of a SOFC could impact the electrochemical performances, from theoretical and experimental points of view. The model results demonstrate that a patterned interfaces along with an electrolyte having a thickness smaller than the dimensions of the pattern, lead to a strong increase of the exchange surface, hence to the exchange currents (up to 64%) with respect to flat interfaces. With the use of laboratory standard ceramic processes, this architecturation was experimented on YSZ-Ni self supported anodes on top of which a thin YSZ electrolyte was deposited. The first electrical tests for such a cell with a non-optimized thickness show an increase of the current density with respect to a cell with flat interfaces, from 130 to 300 mA cm^{-2} at 0.7 V, that is even higher than anticipated by the modelling.

Introduction

As in most technological sectors constituted of multilayer structures (batteries, heat exchangers, catalysis supports, fuel cells, electrolysers, power electronics, electrochemical sensors and filters, separation membranes, gas pumps, …), the exchange surfaces are essential so as to ensure the efficiency of energy conversion. A solid oxide fuel cell (SOFC) is an example of {anode/electrolyte/cathode} multilayered structures the marketing of which is highly delayed due to accelerated ageing of constituent materials in redox cycling, along with a manufacturing cost still too high. Thus, a lowering of the operating temperature of SOFCs, without affecting their level of performances, would allow to meet the requirements of durability, by limiting the reactivity between the materials in contact, as well as cost, making possible the use of metal alloys as interconnectors, much cheaper and much stabler than the lanthanum chromites currently used, and whose mechanical and thermal properties are more suitable for the assembly. Increased performances at relatively lower temperatures are reachable by minimizing energy-consuming (activation, resistance, concentration) overpotentials. From these considerations, it is clear that the development routes to improve SOFCs performances

are globally well identified and would lead to shifting the characteristic i/v curve towards higher potentials and higher current densities. Taking inspiration from the specific design of battery electrodes, and of our preliminary results (1), it is proposed here to explore theoretically and experimentally how the mesoscopic scale corrugation of electrode/electrolyte interfaces could improve the electrochemical performances of an anode supported SOFC. This work relies on the modelling of the effect of the increase of the exchange surface between the cathode and electrolyte on the electrical performance of an SOFC performed by F. Delloro *et al.* (2). This effect being significantly beneficial, the objective of this study consists in optimizing it in relation to the laboratory's facilities for cell fabrication. To that extent, the design of an anode/electrolyte interface having a particular geometrical shape will be studied, and its effect on the performances of the cell be evaluated via the finite element method; the geometrical pattern at interfaces that leads to the best simulated performances will then be implemented through a sequence of shaping processes able to reach as closely as possible this optimum geometry. The electrical properties of a cell with such design of interfaces will be evaluated and compared to that of a cell with flat interfaces.

Electrochemical Modelling

In this part, the previous 2D study of the architectured anode/electrolyte interfaces (1) is generalized to the cases of symmetrical 3D geometric patterns generated from a rectangle, a triangle or an ellipse, namely and arbitrarily a parallelepiped, a pyramid and an ellipsoid (Figure 1). For the parallelepiped-shaped pattern, only the special case of the cube is studied for simplicity. This 3D study is based on the finite element method.

In the modelling, the thickness of the different components was set to 10 μm for the electrolyte, to 400 μm for the supporting anode, and to 100 μm for the cathode. Because of the periodic geometric pattern at interfaces, the effective thickness of both anode and cathode will vary locally by 100 μm, since the maximum depth H of the 3D patterns was fixed at 100 μm (Figure 2). The half-width L of the patterns as well as their spacing D were set at 50 μm in all cases of these geometric shapes. The elements of the electrochemical model, i.e. the constitutive equations, assumptions, simulation parameters, boundary conditions, are detailed in the next section.

Constitutive Equations

The ionic transport, in both electrodes and in the electrolyte, can be described by the following equation:

$$\nabla \cdot \left(\sigma_{YSZ} \times \nabla u \right) = B \times i_v \qquad [1]$$

where u is the ionic potential and σ_{YSZ} the ionic conductivity of YSZ. Different conductivity values (see Table I) were considered for YSZ in the dense electrolyte (σ^{o}_{YSZ}) and in the porous electrodes (σ^{eff}_{YSZ}). The right hand side of the equation, namely the source/sink term, couples the ionic transport with the electrochemical reaction rate. *B* equals 0 in the electrolyte, -1 in the anode and 1 in the cathode and i_v is the volumetric current density, proportional to the local reaction rate.

The Dusty Gas Model (DGM) (3,4) was used to simulate the gas transport. A binary system of gas species is considered in both electrodes (H_2-H_2O in the anode compartment, O_2-N_2 in the cathode chamber). For each gas species i in the compartment, the following behaviour equation can be derived:

$$\nabla \cdot \left(\frac{k_{i,1}}{RT} \times \nabla P_i \right) + \nabla \cdot \left(\frac{k_2}{RT} \times \nabla P_T \right) = S_i \qquad [2]$$

where subscript i runs either in (H_2, H_2O) or in (O_2, N_2), R is the ideal gas constant, T is the operating temperature, P_i is the partial pressure of species i, P_T is the total pressure. S_i is the molar consumption or production rate due to electrochemical reactions (with $S_{H_2} = i_{v,a}/2F$, $S_{H_2O} = -i_{v,a}/2F$, $S_{H_2O} = i_{v,c}/4F$, $S_{N_2} = 0$). The other parameters are given as follows:

$$k_{i,1} = \frac{D_{i,K} \times D_{12}}{D_{12} + D_m}, \qquad k_2 = \frac{D_{1,K} \times D_{2,K}}{P_T \times (D_{12} + D_m)} + \frac{K}{\mu} \qquad [3]$$

$$D_m = x_1 \times D_{2,K} + x_2 \times D_{1,K}, \qquad D_{1,K} = \frac{\varepsilon}{\tau} \times \frac{d_P}{3} \times \sqrt{\frac{8 \times RT}{\pi \times M_i}} \qquad [4]$$

$$\mu = \frac{\mu_1 c_1 M_1^{0.5} + \mu_2 c_2 M_2^{0.5}}{\mu_1 M_1^{0.5} + \mu_2 M_2^{0.5}}, \quad D_{1,K} = \frac{\varepsilon}{\tau} \times \frac{d_P}{3} \times \sqrt{\frac{8 \times RT}{\pi \times M_i}}, \quad M_{1,2} = \frac{2}{M_1^{-1} + M_2^{-1}} \qquad [5]$$

where x_i is the molar fraction, μ_i the viscosity and M_i the molecular weight of gas species i, d_p is the mean pore diameter, ε the porosity and τ the pore tortuosity. V_i is the special Fuller *et al.* diffusion volume. K is the permeability of the porous electrode, evaluated using the Blake-Kozeny relation: $K = (1/(72 \times \tau)) \times (((d_p \times \varepsilon)/(1-\varepsilon))^2$.

$D_{i,K}$ and D_{12} are effective diffusivities for Knudsen and binary diffusion, respectively. All gas-related parameters were extracted in (5). Reactions rates of the electrochemical semi-reactions taking place at each electrode are expressed by the well-known macro-kinetic Butler-Volmer equation:

$$i_v = i_{TPB} \times \lambda_{TPB} \times \left[\exp\left(\frac{\beta \times nF}{RT} \times \eta_{act} \right) - \exp\left(-\frac{(1-\beta) \times nF}{RT} \times \eta_{act} \right) \right] \qquad [6]$$

All the parameters taking part in equation [6] are different in the anode and cathode compartments. i_v (A m^{-3}) is the volumetric current density, coupling the transport equations for gas species and ions as a source/sink term. η_{act} is the local activation overpotential and n the number of electrons involving in the electrochemical half-reaction. β, the transfer coefficient, is assumed to be 0.50. i_{TPB} is the exchange current rate per unit length (A m^{-1}) of TPB and λ_{TPB} the TPB length density (m^{-2}) in the electrode. Empirical equations can be used for the calculation of i_{TPB} for the anode (6) and for the cathode (7) respectively:

$$\text{anode: } i_{TPB} = 31.4 \times P_{H_2}^{-0.03} \times P_{H_2O}^{0.4} \times \exp\left(-\frac{18300}{T}\right)$$

$$\text{cathode: } i_{TPB} = 1.1 \times P_{O_2}^{0.5} \times \exp\left(-\frac{16500}{T}\right) \quad [7]$$

For λ_{TPB}, a value of 1.8×10^{12} m^{-2} was chosen (8-,9,10,11). Activation overpotentials are defined as:

$$\text{anode: } \eta_{act} = \phi_{e,a} - u - E_a, \qquad \text{cathode: } \eta_{act} = E_c - (\phi_{e,c} - u) \quad [8]$$

where ϕ_e and u represent the electronic and the ionic potentials, respectively. E_a and E_c refer to electrode equilibrium potentials, which can be expressed as:

$$E_a = -\frac{RT}{2F} \times \ln\frac{P_{H_2}}{P_{H_2O}}, \qquad E_c = E_{OC} + \frac{RT}{4F} \times \ln P_{O_2} \quad [9]$$

The cell operating voltage ($E = \phi_{e,a} - \phi_{e,c}$) is fixed at 0.70 V for all simulations as a boundary condition. The values of the simulation parameters are given in Table I. After appropriate meshing of the simulation domains, the equation system was solved for the five unknowns (u, P_{H_2}, P_{H_2O}, P_{O_2} and P_{N_2}). The total current produced was then calculated as an integral over the anodic domain AV: $I_T = \int_{AV} i_v \times dxdy$. This value was normalized with respect to the length of the simulation domain to finally get the density of produced current per unit cell length (A m^{-1}).

TABLE I. Simulation parameters.

Parameters	Values
T (temperature)	800 °C
ε (porosity)	anode: 0.33, cathode: 0.50
V_{YSZ} (YSZ vol. frac.)	anode: 0.33, cathode: 0.25
τ_{YSZ} (YSZ tortuosity)	3
σ^{o}_{YSZ} (bulk YSZ conductivity)	$3.34\times10^{4} \times e^{(-10300/T)}$ S m^{-1}
σ^{eff}_{YSZ} (effective YSZ conductivity)	$\sigma^{o}_{YSZ} \times V_{YSZ} \times \tau_{YSZ}$
λ_{TPB} (TPB density length)	1.8×10^{12} m^{-2}
d_p (mean particle diameter)	2 μm

The model established and implemented in the COMSOL Multiphysics® software takes into account masses and charges conservation, gas transport and electrochemical reaction kinetics. In this paper, the focus is put on the local effect caused by each geometrical pattern at the electrolyte/electrode interfaces, and especially on those parameters that play an essential role on the final electrochemical properties of the cell, i.e. the partial pressure of gases (H_2 and O_2) and water pressure on the anode side, hence activation and concentration overpotentials that they lead to, the distribution of the volumetric charge transfer current and finally the i/v characteristics. Since the patterns present a symmetry axis, the properties related to the other cutting planes passing through

this axis are identical to the first order; thus the results of the simulation will be presented in two dimensions.

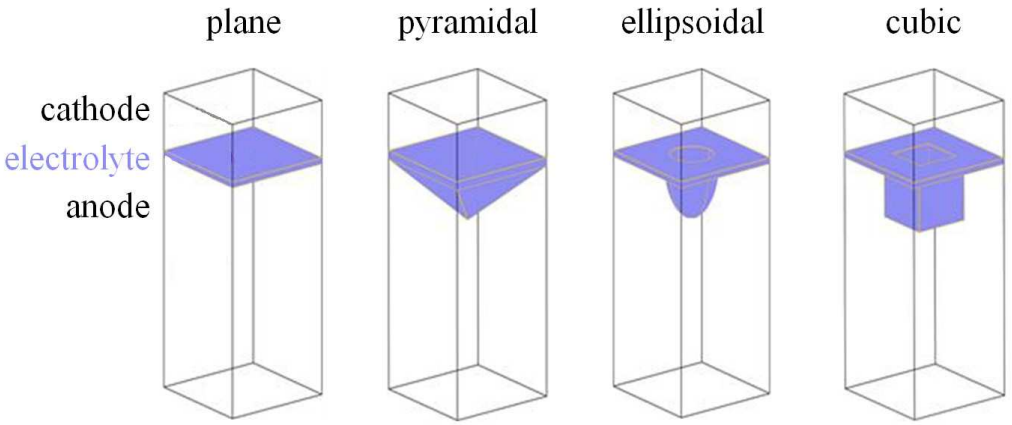

Figure 1. Diagram in 3D of the four interface geometries studied in this work.

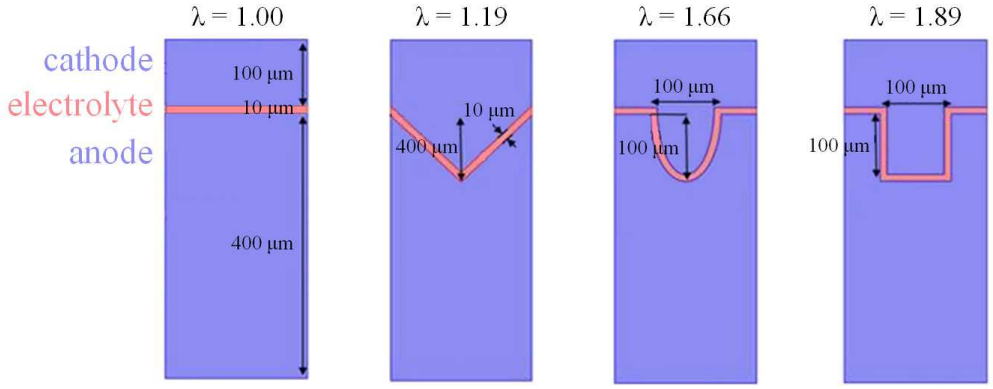

Figure 2. Cross section of the four interface geometries studied and corresponding dimensions of the patterns. The expansion factors defined as the surface of the architectured interface divided by the surface of the plane interface without pattern are indicated above each diagram.

Boundary conditions are summarized in Table II. The boundaries are identified through cardinal points, with reference to the scheme in Figure 2.

TABLE II. Boundary conditions: P is the total pressure, u the ionic potential, e the electronic potential.

Boundary	**Conditions**
Cathode (N)	P = 1 atm (21% O_2 + 79% N_2); grad(u) = 0; e = 0
Anode (S)	P = 1 atm (97% H_2 + 3% H_2O); grad(u) = 0; e = E
On all sides (E,W)	Periodic

Experimental

In this section, the geometric control of the anode/electrolyte interface on the electrochemical performances was experimented on an elementary SOFC in a self-supported anode configuration. The interest of an architectured interfaces will be

validated experimentally by electrical characterization performed on two cells (30 mm in diameter, 570 μm thick), one with flat interfaces considered as reference sample, and the other with architectural interfaces, all other things being equal.

The two cells were prepared according to the following protocol:

(i) six successive layers were deposited by tape casting for the fabrication of the supporting anode;

(ii) after drying under static air for 48 hours, the anode was laminated in two perpendicular directions and its surface architectured by cold stamping using an aluminium mould that was machined to create a periodic truncated pyramid pattern, close to a cube, whose dimensions are as close as possible to those set up in the modelling;

(iii) the electrolyte was deposited in two successive layers by bar coating and then the assembly was co-sintered at 1350°C for 3 hours and then cooled down to room temperature by passing through two plateaux fixed at 1200°C and 1000°C, each maintained for 2 hours. After sintering, the thickness of the composite anode was 500 μm while that of the electrolyte was 10 μm for the reference cell (flat interfaces) and varied from 7 to 15 μm for the architectured sample, the two cells having been manufactured under the same operating conditions;

(iv) a CGO diffusion barrier layer was deposited by bar coating and its thickness was about 2-3 μm after sintering at 1250°C for 3 hours;

(v) identical cathodes in terms of microstructure and thickness were deposited on the CGO diffusion barrier. The LSCF48-CGO composite was chosen as the cathode material due to its lower activation and resistance overpotentials compared to LSCF48. This cathode was deposited on the diffusion barrier and then sintered at 1000°C for 3 hours. The LSCF48-CGO cathode was then covered with a LSCF48 layer as current collector. In both cases, the cathode and the current collector are 50 and 20 μm thick, and the surface of the cathode is 4.5 cm^2.

Current/potential characteristics were recorded using a test bench from FIAXELL (Lausanne, Swiss). A non-destructive sealing was ensured by means of alumino-silicate felts positioned on either side of the cell. On the cathode side, a thin Au grid made up of a fine mesh was used. On the anode side, the contact with the dihydrogen diffuser in inconel was assured by means of a laminated nickel foam. After setting up of the cell, the furnace was preheated at 400°C for 3 hours (heating rate of 200°C h^{-1}) in order to purge the anode compartment and to burn the adhesive which was previously used to fix the cell. When the plateau is reached, the cathode compartment was supplied with synthetic air at a flow rate of 400 mL min^{-1}. The furnace was then heated to 750°C with a heating rate of 300°C h^{-1}, and as soon as the plateau is reached, the anode compartment was fed with hydrogenated argon (5% by volume of H_2) with a flow rate of about 120-130 mL min^{-1} maintained for 24 hours in order to carry out the in-situ reduction of NiO to Ni. After reduction, the anode compartment was supplied with dihydrogen (99.9%), produced by an electrolyzer based on a PEMFC (Polymer Electrolyte Membrane Fuel Cell), with a flow rate of 127 mL min^{-1}. A temperature of 785°C. was programmed in order to reach the desired temperature of 750°C close to the cell. A Kikusui KFM2150 rheostat is connected to the cell in order to modulate the intensity of the current flowing through it, and thus to measure i/v characteristics.

Results and Discussion

Theoretical Analysis of the Effect of Architectured Interfaces on SOFC Performances

Table III presents the results of the 3D simulations carried out at an operating voltage of 0.70 V for the four interface geometries, with the values of the calculated current density for each pattern and the gain provided by a specific pattern with regard to a plane interface, and λ is the surface enlargement factor of the exchange surface for each pattern. These results show that the presence of a periodic cube-shaped pattern leads to the most significant improvement in the current density, of the order of 64%.

TABLE III. Results of 3D simulation under an operating voltage of 0.70 V.

Shape of the pattern	Plane	Pyramidal	Ellipsoidal	Cubic
Interfacial enlargement factor (λ)	1.00	1.19	1.66	1.89
Current density / A cm^{-2}	0.96	1.24	1.28	1.57
Gain (ΔI) / %	0	30	34	64

Effect of the Geometrical Pattern on the Partial Pressure of Gases. Figures 3 and 4 show the various partial distributions of gas, oxygen at the cathode and hydrogen at the anode, and water vapour at the anode. The efficiency of the cell is all the more important as the gases are consumed and the production of water is strong; as a result, the efficiency will be maximal when the gradients of the partial pressure are maximal between the outer edge of the electrodes and the electrolyte. Figure 3 clearly shows that the introduction of a geometric pattern at the electrode/electrolyte interfaces, with respect to plane interfaces, has a significant influence on the intensity and extension of the gradients of partial pressure. Thus, the architecturation strongly facilitates the consumption of oxygen and hydrogen, resulting in a correlated increase in water production.

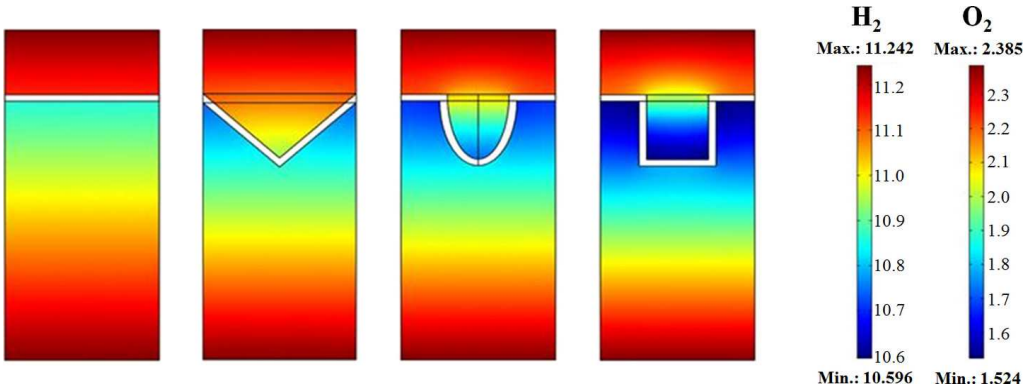

Figure 3. Distribution of partial pressure of gases at the anode and cathode.

Two phenomena affect the distribution of gases in the electrodes. On the one hand, the increase in local densities of the exchange currents near the interfaces leads to a higher consumption or production of gases. On the other hand, the architecturation of the interface induces an elongation of the path the gases have to go to reach or leave the reaction sites, most of which are in the vicinity of the interface. In terms of efficiency, the parallelepiped pattern undoubtedly leads to the highest gradients of oxygen and hydrogen consumption and water production. Figures 3 and 4 illustrates the places close to the patterns where the highest concentration of fuel and oxidizer consumption are recorded

(dark blue zones), which gives valuable indications for practical shaping of the cells. In this case, the zones displaying the highest electrochemical activity coincide with the places far from the gas inlet channels. For example, Figure 4 indicates that oxygen is most strongly consumed at the bottom of the cube, and to a lesser extent on its vertical walls; correspondingly, the places with higher hydrogen consumption are associated with the horizontal inter-pattern segments, and to a lesser extent along the vertical walls of the cube. The water content for its part follows the gradients of hydrogen partial pressure. Interestingly, it can be noted that the zones of higher oxygen consumption do not necessarily correspond to the zones of higher hydrogen consumption. The location of the areas of higher water production is essential in terms of component microstructure since its evacuation must be efficiently ensured by the porous network of the anode without affecting the concentration overpotentials. Figure 4 clearly indicates that the geometric parameters of the pattern, particularly D and H, should be chosen carefully so that the water does not remain confined between the patterns at high current, thus preventing hydrogen from being consumed effectively. Globally, it is found that a high expansion factor λ promotes a high consumption of fuel and oxidizer, and therefore contributes to the efficiency of the cell.

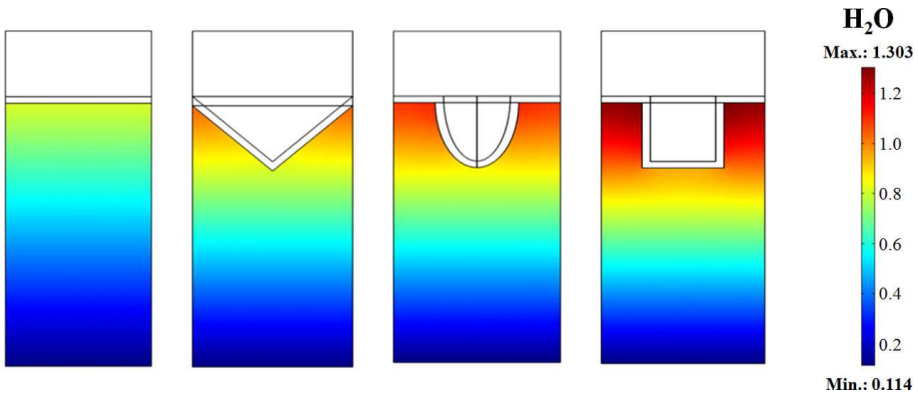

Figure 4. Distribution of partial pressure of water at the anode.

Effect of the Geometrical Pattern on the Activation Overpotential. The distribution of activation overpotentials for each pattern is presented in Figure 5. Overall, the activation overpotential is negligible away from the electrolyte, and essentially varies in its immediate vicinity where it reaches very important values, somewhat higher on the cathode side, which is consistent with the results of the literature (12). For the cathode, the maximum activation overpotential increases from 0.15 V for the flat configuration to 0.19 V for the ellipsoid and the cube, and 0.25 V for the pyramid. For the anode, it ranges from 0.14 V for the flat configuration to 0.20 V for the others. These variations are significantly limited to a layer of about 10 to 20 μm for the anode, and can exceed 50 μm for the cathode in the presence of a pattern. This layer gives a good indication about the active area in each electrode. It will be noted that the maxima of overpotentials are recorded close to the points of strong concavity of the electrolyte for each of the patterns, and that the relative minima, in the vicinity of the interfaces, of the order of 0.10 V at the cathode and 0.05 V at the anode, values lower than those associated with the plane interface, are localized at the points of strong convexity of the electrolyte; this is not surprising because these latter give access to a larger volume of electrode than the high concavity points and thus statistically to a higher number of TPB, which can be interpreted as a more marked local catalytic activity.

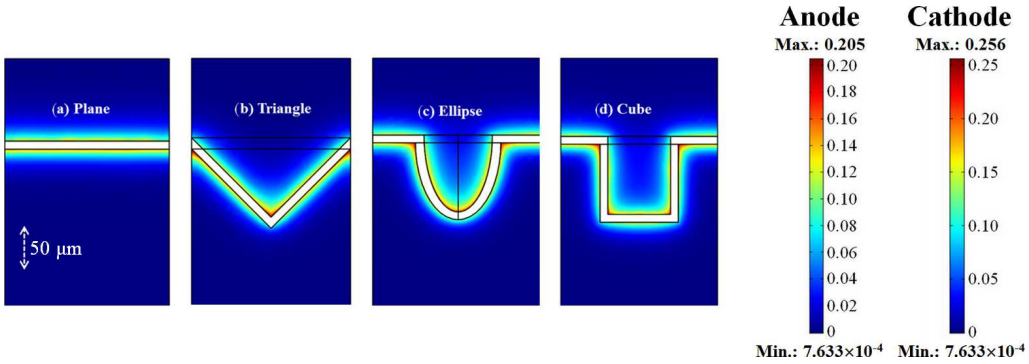

Figure 5. Distribution of activation overpotential at the electrodes.

Effect of the Geometrical Pattern on the Concentration Overpotential. The distribution of concentration overpotentials is shown in Figure 6 for each pattern. Regardless the configuration, the concentration overpotentials are preponderant in the anode, phenomenon typically observed for SOFCs: it reaches 0.09 V for the plane interface. However, on the cathode side, even if the concentration overpotential is low for a plane interface (0.002 V), it increases rapidly (0.004 V for the pyramidal pattern and 0.007 V for the ellipsoidal pattern) with the interfacial expansion factor λ, and reaches 0.01 V for the cubic pattern. In contrast, the concentration overpotential remains high on the anode side, ranging from 0.10 V for the pyramidal pattern to 0.13 V for the cubic pattern. Finally, the concentration overpotential at the anode slightly changes along the interfaces and therefore in the reaction zones whatsoever the pattern; from this point of view and with regard to concentration overpotentials, the choice of the pattern does not appear to be fundamental, which leaves a certain degree of freedom for the shaping of the cells.

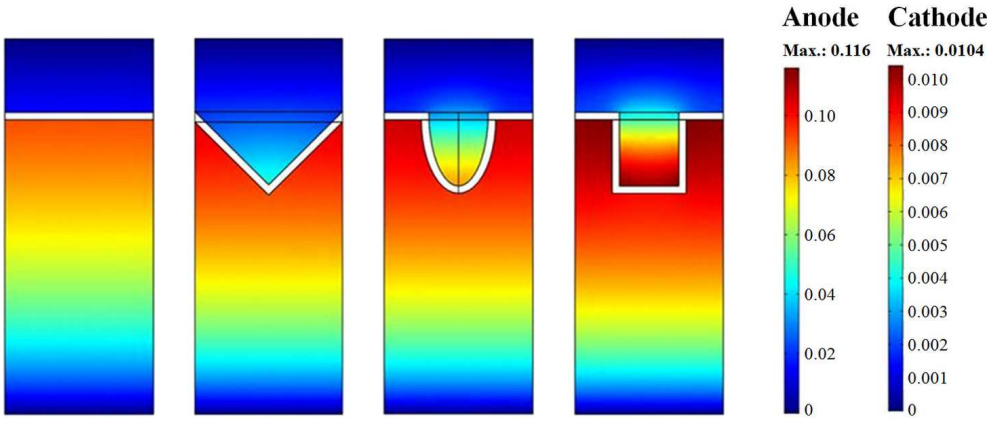

Figure 6. Distribution of concentration overpotentials at the electrodes.

In contrast to activation overpotential, the minimum of concentration overpotentials are recorded for the plane configuration; the gains on the final performances associated with architecturation of the interfaces are therefore not to be sought on the side of the concentration overpotentials for which the patterns at the interfaces have a rather negative effect. It is not surprising that the profile of concentration overpotentials at the anode is quite similar to that of the distribution of partial pressure of water vapour regardless of the pattern, which itself is comparable to that of the hydrogen consumption (proportional

to the inverse of the partial pressure of hydrogen); at high current densities, this is indeed the water vapour which affects the flow of hydrogen towards the reaction points. As previously, the profile of the concentration overpotentials at the cathode clearly reflects the oxygen consumption (proportional to the inverse of the partial pressure of oxygen).

Effect of the Geometrical Pattern on the Distribution of Exchange Currents. Figure 7 displays the distribution of the volumetric exchange currents in the electrodes in the immediate vicinity of the electrolyte for the four geometric patterns. Only the significantly active areas in the 1×10^{8} to 2×10^{9} A m^{-3} range are presented. It is clearly observed that the architecturation of the interfaces, regardless of the pattern, leads to a larger active area compared to a plane interface, especially as the interfacial enlargement factor λ is important. The concave regions, and in particular the internal edges of the patterns where the electrode material is confined, are those where the currents are the highest. The strongest exchange currents appear on the cathode side in areas where the cathode material is confined, then the gain can locally reach a factor of 20 and the active area to can be three times thicker than that of associated with a flat interface. Therefore, the introduction of a geometrical pattern, extending the interfaces and confining the electrode material, is an effective way to involve a significantly higher number of TPB and thus to increase the exchange currents. In the presence of a periodic parallelepipedic pattern, the architectured surface is almost doubled (λ = 1.9) with respect to the flat surface (λ = 1.0), which leads to an improvement of 64% in current density. Even if the concentration overpotentials strongly affects the SOFC performances, their negative effect is widely counterbalanced by the large increase in the exchange currents induced by a greater number of TPBs involved in connection with a higher active volume than for a flat interface.

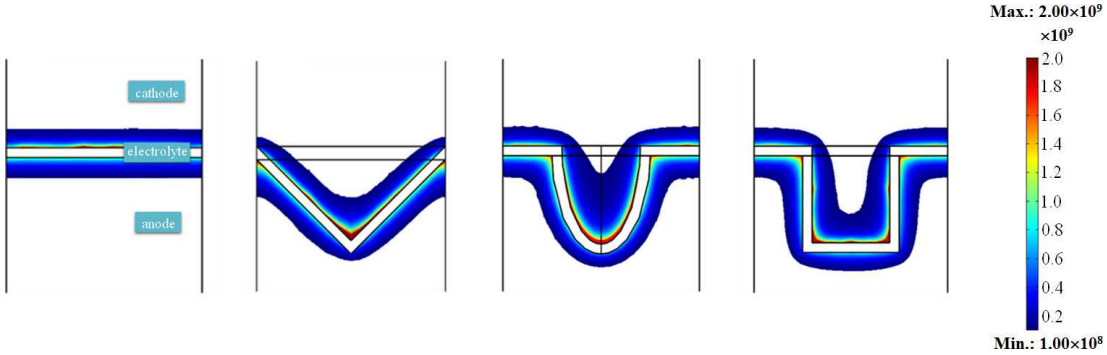

Figure 7. Distribution of volume exchange currents at the electrodes.

Simulated Effect of the Geometrical Pattern on the i/v Characteristic Curve. Figure 8 presents the i/v characteristic curves for the four architectured interfaces. At a typical operating voltage of 0.70 V, it can be seen that the performances can reach 1.6 A cm^{-2} with an architectured electrolyte/electrodes to be compared with a current density of the order of 1.0 A cm^{-2} for a cell with plane interfaces. This ratio of 1.6 is retained over the whole of the voltage range. This curve is interesting for comparison with the literature, or for validation of the model with experimental data.

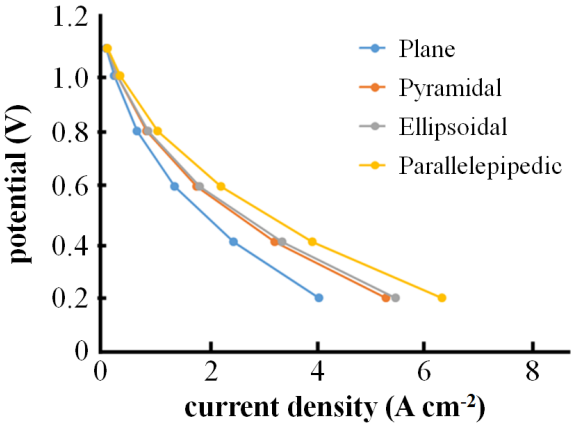

Figure 8. Simulated i/v characteristic curves as a function of the interface geometry.

Comparison between i/v Curves of Cells with Flat and Architectured Interfaces

The i/v characteristic curves of the reference and architectured cells are displayed in Figure 10. The measurement points related to the curve of the reference cell were collected as soon as the anode was entirely reduced. The OCV of the reference cell (0.89 V) at 750°C was slightly higher than that of measured for the architectured cell (0.85 V). The gap was small and could be ascribed to micro-leaks of the felt seals. After recording a first i/v characteristic curve, the equilibrium conditions were restored by opening the external electrical circuit. Concerning the architectured cell (photograph, SEM image and topography of the surface of the anode are displayed in Figure 9), an OCV value at t + 5h identical to that of recorded at t + 3h indicated a stable electrochemical performances.

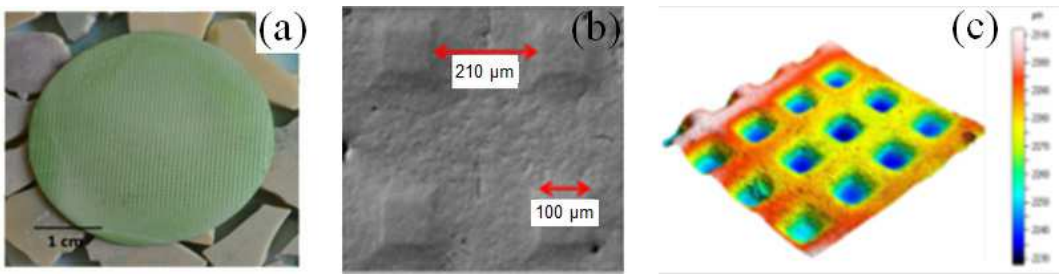

Figure 9. (a) Photograph, (b) SEM image, and (c) topography of the surface of the supported anode.

The subsequent evolution of performances was correlated with the evolution of the reduction of the anode, which was more successful after 5 hours of maintenance in operating conditions. In order to avoid the chemical degradation of the cathode, the electrochemical tests were limited to voltages higher than 0.50 V. At low current, in the area where activation overpotentials are limiting, Figure 10 clearly shows that the catalytic properties of the architectured cell are much better than those of the reference cell, which is totally consistent with a higher number of active TPB involved, and in particular at the cathode where the oxygen reduction reaction is slower than the oxidation of hydrogen at the anode. If there is an inflection of the slope of the curve relative to the reference cell in this region, indicating a significant activation overpotential, nothing is visible for the architectured cell whose behaviour is linear up to the OCV, suggesting that

the activation overpotentials at the electrodes are negligible compared to the ohmic drop which is then preponderant up to the lowest currents. The difference of linear behaviour for the architectured cell with an anode partially or fully reduced suggests that the ohmic drop is related to the evolution of the resistance of the electron conduction pathway in the anode. Globally, it can be concluded that the performances of the architectured cell are much higher than that of the reference cell since, for a typical operating voltage of 0.7 V, current densities of 130 mA cm^{-2} and 300 mA cm^{-2} were measured for the reference and architectured (at t + 5 h) cells, respectively. The architecturation of interfaces thus leads to more than a doubling of performances, while the most optimistic modelling reported above in Table III a 64% increase in performance. The general level of performances, of the order of 200 mW cm^{-2}, remains modest compared to the state-of-the-art since cells displaying current densities of the order of 1.0 to 1.2 W cm^{-2} are developed. However, this work was only focused on the impact of an increase of exchange surfaces on electrical performances.

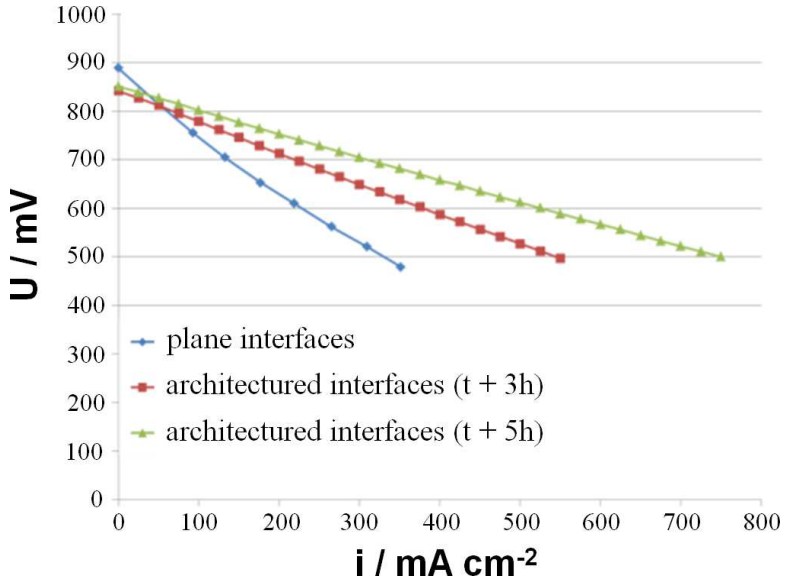

Figure 10. Comparison of i/v characteristic curves of reference and architectured cells.

Conclusion

The effect of the 3D topological corrugation of electrolyte/electrode interfaces of a SOFC was theoretically and experimentally investigated. Three simple periodic geometric patterns were explored, pyramidal, ellipsoidal and cubic, and were compared numerically to a reference flat configuration of interfaces. Modelling shows a clear increase of the performances when the created surface, in excess with regard to the flat configuration, was increased. An improvement of 64% was calculated for the cubic pattern. The modelling allowed to interpreting the effect of the corrugation on different key parameters such as the partial pressure of gases, the concentration and activation overpotentials, the exchange currents. It was seen that the negative effect of the patterns on the overpotentials was strongly counterbalanced by the positive effect on the exchange current, whatever the pattern. The key results were that the improvement was higher when the patterns gave rise to singularity points and to the confinement of the electrode materials inside the pattern, leading to an increased number of TPBs that are solicited,

and effect that is maximal when the width of the pattern is exactly equal to two times the thickness of the active layer in the electrodes. Surprisingly, the experimental validation on a real cell with interfaces architectured with a truncated pyramid, close to a cubic pattern, showed that the measured performances were more than doubled with regard to a cell with flat interfaces. These results are of major importance for the development of SOFC systems.

References

1. M. Geagea, J. Ouyang, B. Chi, F. Delloro, A. Chesnaud, A. Ringuedé, M. Cassir and A. Thorel, in: *Solid Oxide Fuel Cells 14 (SOFC-XIV)*, S.C. Singhal and K. Eguchi, Editors, vol. 68(1), p. 1969-1978, The Electrochemical Society Proceedings Series, ECS Transactions, Pennington, NJ (2015).
2. F. Delloro, M. Viviani, *J. Electroceramics*, **29**(3), 216-224 (2012).
3. S. Kakaç, A. Pramuanjaroenkij, X.Y Zhou, *Inter. J. of Hyd. Energy*, **32**(7), 761-786 (2007).
4. E.A. Mason, A.P. Malinauskas, R.B. Evans, *J. Chem. Phys.*, **46**, 3199-3216 (1967).
5. R. Radhakrishnan, A.V. Virkar, S.C. Singhal, *J. Electrochem. Soc.*, **152**(1), 210-218 (2005).
6. Y. Suzue, N. Shikazono, N. Kasagi, *J. Power Sources*, **184**, 210-218 (2008).
7. R. Radhakrishnan, A.V. Virkar, S.C. Singhal, *J. Power Sources*, **196**, 4911-4922 (2011).
8. A. Konno, H. Iwai, M. Saito, H. Yoshida, *Journal of Power Sources*, **196**, 98-109 (2011).
9. M. Andersson, J. Yuan, B. Sundén, *J. Heat Mass Transfer*, **55**, 773-788 (2012).
10. J. Yuan, Y. Huang, B. Sundén, W.G. Wang, Heat Mass Transfer, **45**, 471-484 (2009).
11. M. Kishimoto, H. Iwai, M. Saito, H. Yoshida, *Journal of Power Sources*, **196**, 4555 (2011).
12. A. Konno, H Iwai, M. Saito and H. Yoshida, *J. Power Sources*, **152**(18), 7442-7449 (2011).